Chem Soc Rev

TUTORIAL REVIEW

View Article Online
View Journal | View Issue

Cite this: *Chem. Soc. Rev.*, 2017, **46**, 5714

Insights into charge carrier dynamics in organo-metal halide perovskites: from neat films to solar cells†

Jiajun Peng,[a] Yani Chen,[a] Kaibo Zheng,*[bc] Tõnu Pullerits[b] and Ziqi Liang*[a]

Organo-metal halide perovskites have recently obtained world-wide attention as promising solar cell materials. They have broad and strong light absorption along with excellent carrier transport properties which partially explain their record power conversion efficiencies above 22%. However, the basic understanding of the underlying physical mechanisms is still limited and there remain large discrepancies among reported transport characteristics of perovskite materials. Notably, the carrier mobility of perovskite samples either in thin films or within solar cells obtained using different techniques can vary by up to 7–8 orders of magnitude. This tutorial review aims to offer insights into the scope, advantages, limitations and latest developments of the techniques that have been applied for studying charge carrier dynamics in perovskites. We summarize a comprehensive set of measurements including (1) time-resolved laser spectroscopies (transient absorption, time-resolved photoluminescence, terahertz spectroscopy and microwave conductivity); (2) electrical transient techniques (charge extraction by linearly increasing voltage and time-of-flight); and (3) steady-state methods (field-effect transistor, Hall effect and space charge limited current). Firstly, the basics of the above measurements are described. We then comparatively summarize the charge carrier characteristics of perovskite-based neat films, bilayer films and solar cells. Finally, we compare the different approaches in evaluating the key parameters of transport dynamics and unravel the reasons for the large discrepancies among these methods. We anticipate that this tutorial review will serve as the entry point for understanding the experimental results from the above techniques and provide insights into charge carrier dynamics in perovskite materials and devices.

Received 29th December 2016

DOI: 10.1039/c6cs00942e

rsc.li/chem-soc-rev

Key learning points

(1) Working mechanisms of perovskites revealed by transient and steady-state techniques
(2) Charge carrier dynamics in perovskite based neat films, bilayer films and operating solar cells
(3) Distinctions of the transport properties between perovskite and conventional thin-film solar cells
(4) Carrier mobility of perovskites with various compositions and nanostructures
(5) Effects of the charge recombination, hot carriers, trap states and phase transition on perovskites

1. Introduction

Organo-metal halide perovskites exhibit a broad optical absorption range, low exciton binding energy and high charge carrier mobility—ideal properties needed for high-performance photovoltaic materials. Up to now, the certified power conversion efficiency (PCE) of perovskite solar cells (PSCs) has soared to ~22.1%,[1] which has largely surpassed that of organic photovoltaic cells and approaches that of crystalline silicon solar cells.

$CH_3NH_3PbI_3$ (denoted $MAPbI_3$) is the earliest and most studied metal halide perovskite in the context of solar energy conversion, yet it exhibits some fatal disadvantages including

[a] *Department of Materials Science, Fudan University, Shanghai 200433, China. E-mail: zqliang@fudan.edu.cn*
[b] *Division of Chemical Physics and NanoLund, Lund University, Box 124, 22100 Lund, Sweden. E-mail: kaibo.zheng@chemphys.lu.se, tonu.pullerits@chemphys.lu.se*
[c] *Gas Processing Center, College of Engineering, Qatar University, PO Box 2713, Doha, Qatar. E-mail: kaibo.zheng@chemphys.lu.se*

† Electronic supplementary information (ESI) available: Table of transport parameters calculated by various transient and steady-state measurements. See DOI: 10.1039/c6cs00942e

moisture, light and thermal instabilities and environmental concerns caused by lead. In order to solve these issues, alternative elements to Pb, various low-dimensional structures and well-ordered single crystals of perovskite materials and their devices with protective outer-layers have been widely investigated. The general chemical formula of perovskites can be written as ABX_3, where A is a monovalent organic or inorganic cation (such as $CH_3NH_3^+$ (MA^+), $HC(NH_2)_2^+$ (FA^+), Cs^+ or their mixtures); B is a divalent metal cation (*e.g.*, Pb^{2+}, Sn^{2+}, Bi^{2+}, Sb^{2+} or their mixtures); and X is a halide anion (*e.g.*, Cl^-, Br^-, I^- or their mixtures).

In the past few years, charge transport dynamics in perovskites has attracted enormous research attention by employing various techniques from laser spectroscopy to electrical measurement. Although some common photophysical features of perovskites such as low exciton binding energy, high charge mobility and long carrier diffusion length have become well-accepted in the community, the quantification of charge carrier parameters remains a daunting task. One of the main reasons is the complexity of the perovskite samples themselves where the synthetic strategies, the film morphologies, and even the ambient atmosphere all play critical roles in charge transport.

Jiajun Peng

Jiajun Peng graduated with a BS in electronic science and technology from Fudan University in 2014. She is currently a postgraduate student in the Department of Materials Science at Fudan University under the supervision of Professor Ziqi Liang. Her research interests focus on the charge transport dynamics of organic and perovskite solar cells. Her hobby is playing the guitar and drawing pictures.

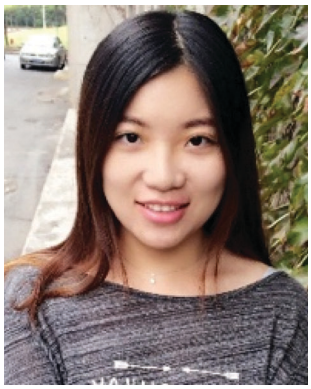

Yani Chen

Yani Chen graduated with a BS in Textile Engineering from Donghua University in 2013. She is currently a PhD candidate in the Department of Materials Science at Fudan University under the supervision of Professor Ziqi Liang. Her research areas focus on perovskite solar cells and organic/inorganic nanocomposite thermoelectrics.

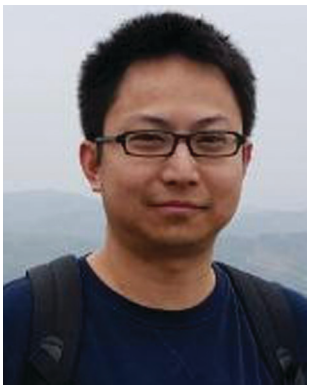

Kaibo Zheng

Kaibo Zheng obtained his PhD from the Department of Materials Science at Fudan University in June 2010. In September 2010, he joined the Chemical Physics Division at Lund University, Sweden, as a postdoctoral fellow. He is currently a senior researcher in chemical physics, Lund University, and double affiliated as a researcher to the Chemical Engineering Dept, Qatar University, Qatar. His research interests include the structure and photophysics of semiconductor and perovskite quantum dot light harvesting materials.

Tõnu Pullerits

Tõnu Pullerits obtained his PhD from the Institute of Physics at Tartu University, Estonia, in 1991. He pursued his postdoc work in Free University of Amsterdam (1992–1993), Umea University (1993–1994), and Lund University (1994). He is currently full professor and head of the Chemical Physics Division at Lund University. He has been a member of the Royal Swedish Academy of Sciences since 2016. His research interests include energy transport in molecular systems, ultrafast charge carrier dynamics and photophysics in photovoltaic materials, and coherence multidimensional spectroscopy.

Ziqi Liang

Ziqi Liang obtained his PhD in polymer science in the Department of Materials Science and Engineering at Pennsylvania State University in March 2006. Then he pursued his postdoctoral work at the University of Cambridge from May 2006 to May 2008. In June 2008, he joined the National Research Energy Laboratory as a postdoctoral researcher and was later promoted to Scientist III. In September 2012, Dr Liang joined the Department of Materials Science at Fudan University as professor. Currently, Prof. Liang's group conducts research encompassing π-conjugated polymers, organic and perovskite solar cells, and organic/hybrid thermoelectrics.

This leads to a large deviation of photophysical parameters---for instance, charge mobilities, lifetimes, diffusion lengths and diffusion coefficients—obtained from even the same experimental technique. The other reason is rarely mentioned or intentionally ignored: different techniques generate systematically distinctive results. For example, the carrier mobilities measured by diverse methods can be 7–8 orders of magnitude different for similar samples. It can highly confuse the readers who would doubt the validity of the results or even the capability of the techniques to truly rationalize the intrinsic properties of perovskite materials.

The objective of this tutorial review is therefore to provide insight into the scope of applicability and limitations of various techniques that are utilized to study charge carrier dynamics in perovskites. We will analyse a range of transport measurements for perovskite based neat films and devices, including (1) four transient laser spectroscopies (based on photo-induced luminescence, optical absorption, terahertz absorption, and microwave conductivity); (2) two electrical transient methods (based on charge extraction by linearly increasing the voltage and time-of-flight); and (3) three steady-state electrical measurements (based on charge transport in field-effect transistors, the Hall effect and space charge limited current). Subsequently, we will first introduce the basic observations obtained by the above techniques on perovskites. Next, the common charge transport features extracted using these methods in neat films, bilayer films and solar cells will be summarized. Finally, we will compare different approaches in evaluating the basic carrier parameters (*e.g.*, charge mobilities) and discuss what account for the discrepancies among these results.

2. Transport measurements of perovskites

2.1 Films without electrodes

2.1.1 Transient absorption (TA) spectroscopy. TA, also known as pump–probe spectroscopy, is a well-established technique to monitor the ultrafast dynamics of photo-induced processes in molecular or semiconductor systems. In brief, it involves excitation of the sample with a short (from a few femtoseconds to a few tens of picoseconds) laser pump pulse, followed by a weak time-delayed monochromatic or broadband white light continuum (WLC) probing pulse which measures the pump-induced absorption changes of the sample. This method can cover a very wide range of timescales (10^{-13}–10^{-4} s) and is sensitive to almost any photo-generated species (*e.g.*, free charges, excitons, polarons, *etc.*) in perovskites. Yet, it also brings up a critical challenge to distinguish individual contributions of these species in the case of overlapping spectral features. In perovskite studies, TA is safe to independently analyse the photo-physics in relatively simple systems (*e.g.*, single crystals, trap free films, *etc.*). However, when the system dynamics are complicated by multiple photo-physical processes and complex morphologies, additional information obtained using other techniques would be needed for constructing a unique kinetic model.

As depicted in Fig. 1A, a typical TA spectrum of $MAPbI_3$ after photo-excitation consists of two negative photobleach bands, termed PB1 and PB2, at 760 nm and 480 nm, respectively, and one broad positive excited state absorption band (namely, EA1) in-between in the visible region. It is widely accepted that PB1 corresponded to the state filling which blocked the optical transition from the valence band maximum (VBM) to the conduction band minimum (CBM) of perovskites.[2] An additional weak bleach tail at the red curve of PB1 was a characteristic feature of sub-band gap trap states.[3] The TA spectrum of the $MAPbI_3$ film in the near-infrared (IR) region exhibited broad non-structured absorption which is attributed to free carriers in the CB (EA2). In the IR region, the two bands at 900 and 1480 cm^{-1} with dispersive line-shapes were assigned to the Fano resonances between the vibrational transitions of the MA cation and the quasi-continuous intra-CB transition (Fig. 1B).[4]

PB1 was correlated with the population of excited charges at the band edge. The decay time (τ) of PB1 in the $MAPbI_3$ neat film strongly depended on the trap density of the film which varied by the synthetic methods (*e.g.*, one-step or two-step solution and vapour deposition processes) and the resulting uniformity and crystallinity of the film. A wide range of lifetimes from hundreds of picoseconds to tens of nanoseconds

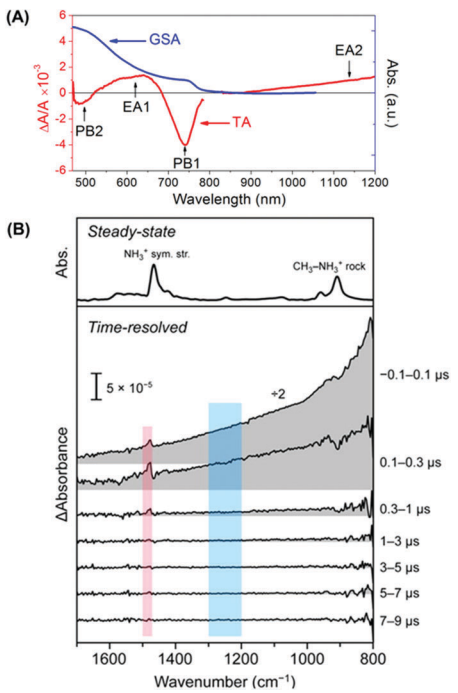

Fig. 1 (A) Typical spectral features of a TA spectrum (red curve) of an $MAPbI_3$ film directly after photoexcitation together with its ground-state absorption (GSA) spectrum (blue curve). (B) TA spectra in the near-IR region revealing the Fano resonances between the vibrational transitions of the MA cation and the quasi-continuous intra-CB transition (red region). Reproduced with permission: (B) from ref. 4. Copyright 2016, American Chemical Society.

can be found in the literature.[5] Remarkably, a mixed-halide $MAPBI_xCl_{1-x}$ film generally exhibited a much longer charge carrier lifetime ($\tau > 100$ ns) because of its significantly smaller trap density.[6]

In well-crystalized perovskite samples where surface recombination is dominant, TA kinetics can be well fitted by a one-dimensional diffusion model to provide the diffusion coefficient (D) of photo-generated charge carriers.[7] By this means, the D value was calculated to be 0.27 $cm^2\ s^{-1}$ for $MAPbBr_3$ single crystals. On the other hand, by applying the spatial mapping in the TA measurement, the charge transport can be followed in real space, allowing direct evaluation of D. From such TA microscopy experiments, a D value of 0.05–0.08 $cm^2\ s^{-1}$ was achieved in an $MAPbI_3$ thin film.[8] D also depended on the trap density of the perovskite and differed from the values obtained using other techniques which will be discussed in the next section.

2.1.2 Time-resolved photoluminescence (TRPL) spectroscopy. TRPL is measured by exciting a sample with a pulsed light source, and recording the intensity of photoluminescence (PL) as a function of time from the excitation. The PL is proportional to the population of the emitting states and therefore it reports directly on the dynamics of photo-generated charges in a semiconductor.

The PL lifetimes of ~10 ns in $MAPbI_3$ films and >100 ns in $MAPbI_xCl_{3-x}$ films corresponded to the decay of the charge carrier population.[4–6] Modelling of the PL dynamics by one-dimensional carrier diffusion, the consequent diffusion length (L_D) was estimated to be ~100 nm for $MAPbI_3$ polycrystalline films with $D = 0.017\ cm^2\ s^{-1}$ for electrons and $0.011\ cm^2\ s^{-1}$ for holes.[9] In mixed-halide $MAPbI_xCl_{3-x}$ films, the L_D can reach 1 μm with $D = 0.04$–$0.05\ cm^2\ s^{-1}$.[10] The charge transport was proven to be more efficient in larger grain-sized films with $D = 0.1$–$2.5\ cm^2\ s^{-1}$.[11] This indicates that the carrier transport in perovskites is strongly modulated by trap density—especially by the surface/interface defect states. In addition, from the D values, the mobilities of minority carriers can be evaluated to be 10^{-1}–$10^{-2}\ cm^2\ V^{-1}\ s^{-1}$.[11]

Owing to a wide variety of detection configurations—for instance, photodiodes, streak cameras, or photomultiplier tube (PMT) set ups for up-conversion or single-photon counting—with different time and spatial resolutions (*e.g.*, in PL microscopy) together with spectral responses, TRPL is one of the most popular tools for studying charge dynamics in perovskite materials. However, some non-radiative recombination kinetics in perovskites cannot be detected in TRPL. The probed emission can also be influenced by re-absorption or photo-recycling processes.[12] Therefore, the extraction of intrinsic photophysics using TRPL is always limited.

2.1.3 Time-resolved terahertz absorption spectroscopy (TRTS). A terahertz (THz) wave with a photon energy in the 1–100 meV range can be responded by the low-energy excitations of photo-generated charges in terms of carrier generation, scattering and lattice vibrations. Therefore, TRTS can probe the photo-induced charge carrier dynamics in semiconductors where the transient alternating current (AC) conductivities can

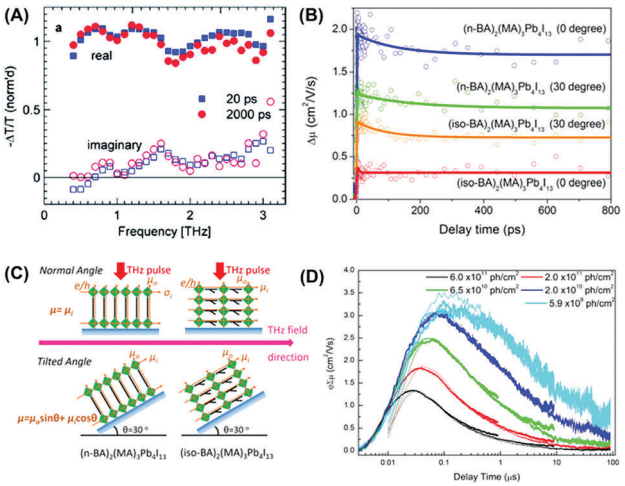

Fig. 2 (A) Complex TRTS spectra of $CH_3NH_3Pb_{3-x}Cl_3$ films. (B) The photoconductivity kinetics from TRTS for 2D perovskite films with different pump–probe geometries under both normal position (*i.e.*, the sample is parallel to the incident THz field polarization, $\theta = 0°$) and tilted angle ($\theta = 30°$) conditions. (C) Schematic of the composition of the charge mobility to be detected by TRTS with different incident angles of THz probe pulses for two samples. (D) Typical TRMC kinetics of $MAPbI_3/Al_2O_3$ films with different excitation intensities. Reproduced with permission: (A) from ref. 14. Copyright 2015, Nature Publishing Group. (B and C) From ref. 18. Copyright 2017, John Wiley & Sons, Inc.

be extracted from the THz absorption.[13] In semiconductors, the dominant photo-induced species are mobile carriers, and the AC photoconductivity spectrum can be well described by the Drude model. Fig. 2A shows the typical frequency-dependent photoconductivity spectra of perovskite films where Drude-like line-shapes can be observed, indicating the formation of free charge carriers directly after photo-excitation.[14] The change in photo-conductivity ($\Delta\sigma$) probed in TRTS can also be expressed as eqn (1):

$$\Delta\sigma = -\frac{\Delta E_{exc}}{E_{gs}}\frac{\varepsilon_0 c}{d}(n_1 + n_2), \quad (1)$$

where ΔE_{exc} is the change in the THz electric field transmitted through the sample after photo-excitation, while E_{gs} is the transmitted THz electric field without excitation (*i.e.*, in the ground state), ε_0 is the permittivity of vacuum, c is the velocity of light, d is the sample thickness, and n_1 and n_2 refer to the refractive indexes of the medium (air) and the quartz substrate, respectively ($n_1 = 1$, $n_2 = 1.5$). The initial carrier mobility (μ) can be calculated from the THz conductivity ($\Delta\sigma$) as shown in eqn (2):

$$\mu = \frac{\Delta\sigma}{\xi n_{exc} e_0}, \quad (2)$$

where ξ is the quantum yield of charge generation, n_{exc} is the excitation density, e_0 is the elementary charge. By combining eqn (1) and (2) and calculating the excitation density by the sample absorbance, μ can be expressed as eqn (3):

$$\mu = -\frac{\Delta E_{exc}}{E_{gs}}\frac{\varepsilon_0 c}{\xi F e_0}(n_1 + n_2)\frac{1}{1 - e^{-\alpha d}}, \quad (3)$$

where F is the excitation fluence in ph per cm^2 per pulse and α is the absorption coefficient.

The initial charge mobility extracted immediately after photoexcitation in perovskites was processed by the above described strategies and generally fell within the 1–100 $cm^2\ V^{-1}\ s^{-1}$ range with strong sample dependence. Taking lead iodide perovskite as an example, the mobility of an $MAPbI_3$ neat film was 35 $cm^2\ V^{-1}\ s^{-1}$,[15] which was slightly higher than $MAPbI_3$ embedded within mesoporous Al_2O_3 measured by both us (20 $cm^2\ V^{-1}\ s^{-1}$)[16] and other researchers ($\sim$8 $cm^2\ V^{-1}\ s^{-1}$).[17] In single crystals, a much higher charge mobility of 800 $cm^2\ V^{-1}\ s^{-1}$ was achieved.[13] Such deviation of carrier mobility may result from scattering from impurities or crystal boundaries varying in the above-mentioned forms of perovskites. On the other hand, the influence of the carrier density on charge mobility should not be neglected. The inter-carrier scattering might be enhanced with high charge density, which led to reduced mobility.[13]

The THz field is always polarized perpendicular to the incident pulse propagation direction. Consequently, the charge mobility in TRTS reflects the carrier motion in the direction perpendicular to the THz beam. In this way, TRTS can discriminate between the contributions of the charge mobility in different spatial directions by varying the incident angle of the THz wave. Very recently, we used such angle-dependent TRTS measurements to obtain the charge mobility within different directions in emerging two-dimensional (2D) Ruddlesden–Popper perovskites (Fig. 2B and C), which are much more moisture-resistant than traditional three-dimensional (3D) perovskites.[18] The angle-dependent photoconductivity in TRTS clearly manifested the preferential orientation of 2D perovskite sheets in $(n\text{-BA})_2(MA)_3Pb_4I_{13}$ and $(\text{iso-BA})_2(MA)_3Pb_4I_{13}$ samples.

In sum, TRTS that selectively monitors photoinduced free charge carriers with the capability of characterizing carrier mobilities is highly relevant for photovoltaic applications. It is a noncontact characterization method where the sample is not influenced by electrodes. However, it should be noted that the extraction of the charge mobilities in TRTS depends strongly on the theoretical model. In the bulk film of perovskites, the well-established Drude-like model is applicable. In nanostructured systems, however, the physically justified mathematical models for TRTS signals have yet to be fully rationalized.

2.1.4 Time-resolved microwave conductivity (TRMC) method. Similar to TRTS, the aim of the TRMC method is also to trace the time evolution of the photoconductivity change $\Delta\sigma(t)$ in the sample after excitation. In the TRMC method, the relative change of the microwave power $\Delta P(t)/P$ is measured and analyzed as eqn (4):[19]

$$\frac{\Delta P(t)}{P} = A\Delta\sigma(t) = Ae(\Delta n_e(t)\mu_e + \Delta n_h(t)\mu_h), \qquad (4)$$

where n_e and n_h are the populations of the mobile electrons and holes, respectively; μ_e and μ_h are the mobilities of electrons and holes, respectively; A is the sensitivity factor dependent on the microwave frequency and on the electrical conductivity of the sample.

Given the lower frequency and longer apparatus response time, the TRMC method probes much slower timescales of dynamics than TRTS. The time-window of TRMC experiments is ns–ms, which is quite suitable for studying the charge carriers in perovskite materials (Fig. 2D). The initial TRMC measurements on the one-step prepared $MAPbI_3$ neat film and $MAPbI_3$ within mesoporous Al_2O_3 scaffolds unveiled long-lived mobile carriers with lifetimes up to 1 μs.[16] The reported charge mobility ($\sim$3 $cm^2\ V^{-1}\ s^{-1}$) was somewhat lower than that in TRTS ($\sim$25 $cm^2\ V^{-1}\ s^{-1}$). Later studies revealed a strong sample dependence of the charge dynamics extracted from TRMC. In two-step fabricated $MAPbI_3$ neat films, the TRMC mobility ($\sim$20 $cm^2\ V^{-1}\ s^{-1}$) is analogous to the above-mentioned one-step fabricated samples. However, a much larger imbalance between electron and hole mobilities was found with $\mu_h/\mu_e = 30$.[20] A higher charge mobility of 30 $cm^2\ V^{-1}\ s^{-1}$ was measured in $MAPbI_xCl_{3-x}$ films with L_D = 10 μm.[21] This was suggested to be facilitated by the lower trap densities. In a single crystal sample, by contrast, a much longer carrier lifetime ($\sim$15 μs) was observed with $L_D > 50$ μm.[22] This was again ascribed to a very low trap concentration, which was 2 orders of magnitude lower in single crystals than in polycrystalline films.

The main differences between the TRMC method and TRTS are the frequency and time resolution. Complementary utilization of TRTS and the TRMC method provides the charge carrier dynamics within a broader time range. However, as an indirect photoconductivity measurement, TRMC is constrained by the need for a theoretical model for data analysis, the same as TRTS.

2.2 Devices with electrodes

2.2.1 Charge extraction by linearly increasing voltage (CELIV) method. The CELIV method can be used to measure charge mobility and investigate the recombination process in working solar cells; however, it cannot distinguish the type of charge carrier—hole or electron. To measure charge mobility, a triangle voltage is applied to extract the intrinsic or photogenerated carriers by dark or photo-CELIV, respectively. The carrier mobility can be calculated using eqn (5):

$$\mu = \frac{2d^2}{3\frac{\Delta U}{\Delta t}{t_{max}}^2}, \qquad (5)$$

where μ is the carrier mobility, d is the thickness of the active layer, $\Delta U/\Delta t$ is the voltage ramp of the applied triangle voltage pulse, and t_{max} is the time when the value of the current density is maximum.

The CELIV method is mostly employed to obtain the charge mobility of various working PSCs and qualitatively investigate the charge extraction and recombination processes. We first applied the CELIV method to investigate the transport dynamics of one-step fabricated neat $MAPbI_3$ and $MAPbI_3$/PCBM bilayer solar cells (Fig. 3A).[23] Upon insertion of the PCBM layer, the charge mobility of $MAPbI_3$ was doubled from 3.2×10^{-4} to 7.1×10^{-4} $cm^2\ V^{-1}\ s^{-1}$ at room temperature.

The device configuration and operation conditions greatly impact the charge transport process of PSCs. Jae-Wook Kang and coworkers studied the relationship between the low-temperature

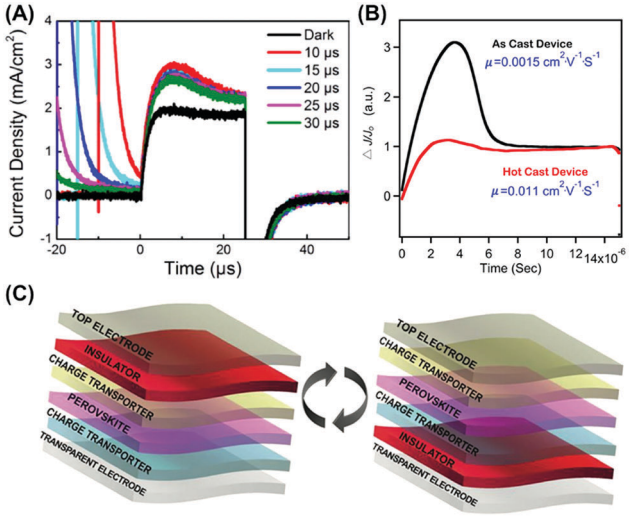

Fig. 3 CELIV measurements of (A) a one-step fabricated neat $MAPbI_3$ device and (B) 2D $(n\text{-}BA)_2(MA)_3Pb_4I_{13}$ devices without and with the hot casting method. (C) Device architecture of the carrier selective photo-CELIV measurement of $MAPbI_3$. Reproduced with permission: (A) from ref. 23. Copyright 2015, American Chemical Society. (B) From ref. 25. Copyright 2016, Nature Publishing Group. (C) From ref. 27. Copyright 2017, John Wiley & Sons, Inc.

transport behavior and performance of two-step fabricated $MAPbI_3$ solar cells.[24] As the temperature was cooled down from 298 to 253 K, the PCE was increased from 14.2% to 15.5% with a noticeable increase of both J_{SC} and V_{OC}, which was due to an increase of the CELIV mobility from 0.67×10^{-3} to 1.07×10^{-3} $cm^2\ V^{-1}$.

Recently, the hot-cast (HC) method was employed to remarkably increase the out-of-plane crystallization of 2D $(n\text{-}BA)_2(MA)_3Pb_4I_{13}$ perovskites and hence achieved a record high PCE of 12.52% in PSCs.[25] By measuring the dark-CELIV as shown in Fig. 3B, it was confirmed that the mobility of the HC device ($0.011\ cm^2\ V^{-1}\ s^{-1}$) was significantly higher than that of the room-temperature cast device ($0.0015\ cm^2\ V^{-1}\ s^{-1}$), suggestive of forming continuous charge transport channels between 2D $\{(MA)_{n-1}Pb_nI_{3n+1}\}^{2-}$ slabs and device electrodes after using the HC method. In order to further increase the out-of-plane orientation of 2D perovskites, we replaced the linear spacer cations ($n\text{-}BA^+$) with short branched-chain ones (iso-BA^+).[18] As a result, $(iso\text{-}BA)_2(MA)_3Pb_4I_{13}$ solar cells exhibited a balance of hole and electron mobilities around 10^{-4} $cm^2\ V^{-1}\ s^{-1}$ yet more nondispersive charge transport as compared to those based on $(n\text{-}BA)_2(MA)_3Pb_4I_{13}$.

In addition to carrier mobility measurements, CELIV can be used as a reliable and facile method to measure the capacitance and dielectric constant of perovskite based devices. For instance, Qianqian Lin *et al.* systematically investigated the electro-optics of $MAPbI_3$-only planar devices.[26] They employed spectroscopic ellipsometry to accurately quantify the refractive index (n) and extinction coefficient (k) of thermally evaporated $MAPbI_3$. On the basis of these results, the real part of the static dielectric constants (ε) was determined to be *ca.* 70 by using the CELIV method and based on the equation $\varepsilon = j_0 d/\varepsilon_0 A$, where j_0 is the displacement current, d is the thickness of the active layer, ε_0 is the vacuum permittivity and A is the triangle voltage ramp (dU/dt).

More recently, a modified photo-CELIV method was taken to separately measure the hole and electron mobilities of perovskites by inserting a 100 nm-thick MoO_3 layer in front of the selected electrodes to block the unwanted type of carrier.[27] To uncover the effect of the device structure on transport dynamics, mesoporous and inverted planar $MAPbI_3$ devices were comparatively investigated as shown in Fig. 3C. Highly balanced charge mobilities were obtained in mesoporous devices, while the hole mobility was lower than the electron mobility in planar devices by half an order of magnitude because the hole injection capability of PEDOT:PSS was inferior to that of the spiro-OMeTAD interlayer.

A unique advantage of the CELIV method is that it can probe the charge transport process directly in working PSCs. By applying both dark and light CELIV, the mobilities of intrinsic and photo-generated charge carriers can be measured, respectively. Thus, CELIV enables investigating the impact of different charge transport layers (*e.g.*, PCBM, PEDOT:PSS, spiro-OMeTAD, TiO_2, *etc.*) or various fabrication processes (*e.g.*, thermal and solvent annealing, solvent additives) on carrier mobility and charge recombination. The only limitation of CELIV is that it only measures the overall charge mobility without distinguishing whether hole or electron carriers.

2.2.2 Time-of-flight (TOF) method. The TOF method can measure both hole and electron mobilities separately and determine different levels of trap states, while light illumination and relatively thick films (>500 nm) are required to ensure that charge carriers traverse the depletion region to reach accurate mobility values. In TOF measurements, fixed positive and negative biases are applied to measure hole and electron mobilities, respectively. The TOF mobility can be calculated from eqn (6):

$$\mu = \frac{d^2}{V \cdot t_{tr}}, \tag{6}$$

where μ is the charge mobility, d is the thickness of the active layer, V is the voltage bias, and t_{tr} is the transient time.

The TOF has been demonstrated as a useful method to measure individual carrier mobility while unraveling trapping states. We initially utilized TOF to unveil the efficient and balanced charge transport in working $MAPbI_3$ PSCs.[23] The hole and electron mobilities of one-step fabricated $MAPbI_3$/PCBM bilayer solar cells were measured to be 5.4×10^{-4} and 4.5×10^{-4} $cm^2\ V^{-1}\ s^{-1}$, respectively, which were higher than those of devices without PCBM. Furthermore, we investigated the effects of both light soaking and phase transition on the charge transport dynamics of two-step fabricated $MAPbI_3$ PSCs (Fig. 4A).[28] It was found that both hole and electron mobilities were gradually increased upon light soaking (Fig. 4B). Meanwhile, rapid changes in hole and electron mobilities were observed during the phase transition from the tetragonal to cubic phase of perovskites.

Apart from those of polycrystalline perovskites, the carrier mobilities of perovskite single crystals can be measured by the

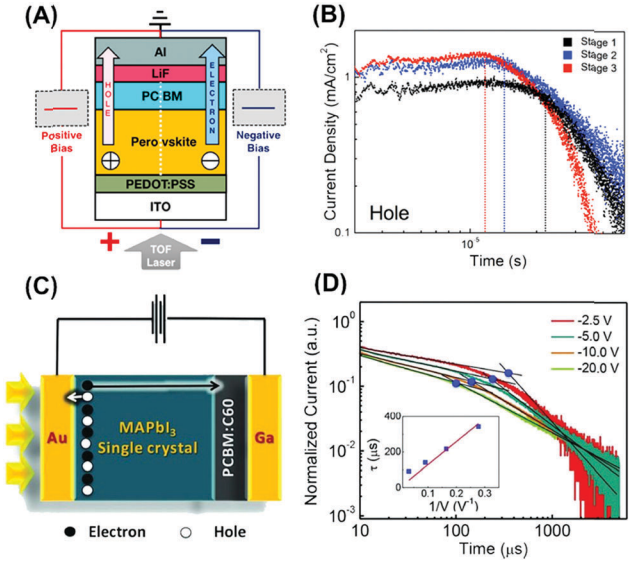

Fig. 4 Schematic TOF measurements and results of (A and B) two-step fabricated $MAPbI_3$ solar cells upon continuous light illumination and (C and D) $MAPbI_3$ single crystal based devices. Reproduced with permission: (A and B) from ref. 28. Copyright 2016, American Chemical Society. (C and D) From ref. 30. Copyright 2015, American Association for the Advancement of Science.

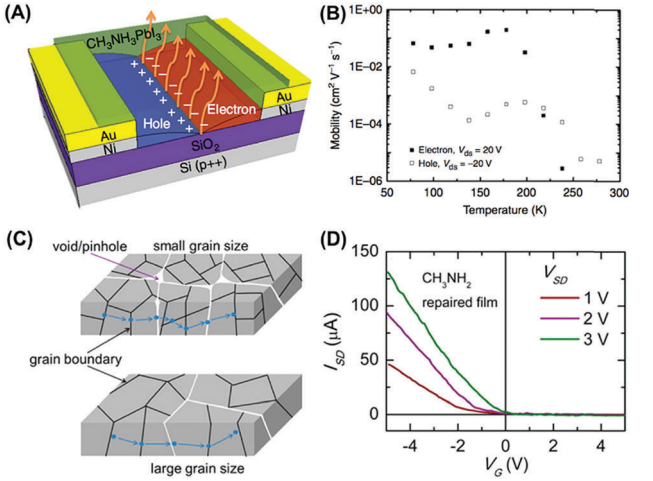

Fig. 5 FET measurements of (A and B) $MAPbI_3$ perovskites at different temperatures and (C and D) CH_3NH_2 treated $MAPbI_3$ perovskites at room temperature. Reproduced with permission: (A and B) from ref. 31. Copyright 2015, Nature Publishing Group. (C and D) From ref. 32. Copyright 2016, American Chemical Society.

TOF method. A method of anti-solvent vapor-assisted crystallization was originally reported by the Bakr group to fabricate large and crack-free $MAPbX_3$ (X = Br or I) single crystals.[29] To conduct the TOF experiments, top transparent ITO and bottom MoO_3/Au/Ag stack electrodes were deposited on both surfaces of perovskite single crystals, respectively. For the first time, the bulk hole mobility of $MAPbBr_3$ single crystals was determined to be 115 $cm^2\ V^{-1}\ s^{-1}$. Meanwhile, the Huang group reported solution-grown $MAPbI_3$ single crystals, yielding unprecedentedly longer electron–hole diffusion lengths over 175 μm.[30] By constructing the Au/$MAPbI_3$ single crystals/PCBM:C_{60}/Ga device as shown in Fig. 4C, the TOF electron mobility was determined to be 24.0 $cm^2\ V^{-1}\ s^{-1}$ with negligible trap states (Fig. 4D). Note that the thickness of the Au electrode was controlled to be 25 nm to ensure both high light transparency and conductivity.

The TOF method is a powerful technique with electrode contacts to measure both hole and electron mobilities in the same device architecture, which is applicable to perovskite single crystals and polycrystalline films. Moreover, the distribution of shallow and deep traps in perovskites can be clearly differentiated by observing different plateaus in TOF j–t curves.

2.2.3 Field-effect transistor (FET) technique. Different from the above out-of-plane measurements, the FET technique enables studying charge transport dynamics in the in-plane direction. Although no charge blocking layer is needed in the FET architecture, the crystallization and quality of perovskites need to be high enough to observe the obvious field effect.

Enormous attention was recently paid towards how to accurately measure and effectively enhance the FET mobilities of $MAPbI_3$ perovskites. For instance, in order to unveil the intrinsic charge transport, $MAPbI_3$ based FETs were studied in a low temperature range of 78–198 K to eliminate the ionic transport induced screening effect (Fig. 5A).[31] As the temperature was decreased below 200 K, both the hole and electron mobilities of $MAPbI_3$ were increased by two orders of magnitude to 2.1×10^{-2} and $7.2 \times 10^{-2}\ cm^2\ V^{-1}\ s^{-1}$, respectively (Fig. 5B). At room temperature or without light illumination, however, $MAPbI_3$ FETs often exhibited poor performance with very low charge mobilities around $10^{-4}\ cm^2\ V^{-1}\ s^{-1}$. To solve this problem, the Ji group applied methylamine (CH_3NH_2) gas treatment on $MAPbI_3$ at room temperature.[32] It was found that such treated $MAPbI_3$ displayed enlarged grain size (Fig. 5C) and hence the FET mobility was doubled to 22.75 $cm^2\ V^{-1}\ s^{-1}$ (Fig. 5D).

Newly developed perovskite microplates also exhibited better FET performance than the polycrystalline analogues. The Duan group innovatively reported the patterned growth of regular and large arrays of $MAPbI_3$ microplate crystals.[33] By thermal annealing treatment, a transformation from n- to p-type semiconductors was clearly observed due to the degradation of perovskites. Meanwhile, these crystals showed a noticeable decrease of both charge mobility and source–drain current in FETs after thermal annealing, which was attributed to the enhanced scattering between charge carriers and defects.

FET measurements can not only measure charge mobility in the in-plane direction, but also quickly determine whether the perovskite samples are n-, p-type or ambipolar semiconductors. Unfortunately, the FET mobility is strongly dependent on the operation temperature, the grain size and even the interfacial morphology of samples. Therefore, the FET method is more applicable to perovskites with high crystallinity and purposely modified electrode surfaces in order to derive intrinsic charge mobility.

2.2.4 Hall effect technique. The Hall effect technique is considered as a reliable steady-state method to determine the intrinsic defect concentration and distinguish whether the

measured semiconductor is n- or p-type. The bulk mobilities of both hole and electron carriers can be measured using the Hall effect method, which is distinct from the above three methods (CELIV, TOF, FET) that measure charge mobility only in a fixed direction.

In 2013, the Hall effect measurement was applied to interpret why lead-free $MASnI_3$ perovskites possessed the band structures of intrinsic semiconductors yet exhibited metal-like high conductivity.[34] A hole concentration of 9×10^{17} cm^{-3} with a high Hall mobility of 200 cm^2 V^{-1} s^{-1} at 250 K was observed in undoped $MASnI_3$ single crystals (Fig. 6A and B). Moreover, the carrier concentration can be further increased by hole doping without affecting the Hall mobility. This phenomenon indicated that $MASnI_3$ was a spontaneously doped semiconductor rather than a semimetal.

Lead based perovskites, however, presented much lower intrinsic carrier concentration than Sn-based perovskites. In 2014, the Huang group performed Hall effect measurements to reveal the p-type behavior of an $MAPbI_3$ film grown by the interdiffusion method.[35] Meanwhile, they observed a low hole concentration of 4–10 $\times$ 10^{13} cm^{-3}, which may arise from the presence of Pb deficiency in perovskites caused by extra MAI supply during the interdiffusion process. In addition, the Hall mobility of perovskites can be reduced by 3 times after inserting the PCBM top layer.

It is worth noting that both perovskite polycrystalline films and single crystals exhibited distinctive transport behavior. To unravel the underlying physical mechanisms, the Podzorov group systematically studied the intrinsic Hall effect in vapor- and solution-grown $MAPbI_3$ films and $MAPbBr_3$ single crystals.[36] The obtained Hall mobilities range from 0.5 to 60 cm^2 V^{-1} s^{-1}, which were closely correlated with the composition and crystallinity of perovskites.

In light of thermally driven phase transitions in perovskites, temperature dependent resistivity and Hall effect measurements were carried out in $MAPbBr_3$ single crystals.[37] A notable increase of conductivity by 4 orders of magnitude was achieved when the insulating perovskite single crystal was electrically biased. Such more conductive states allowed the Hall effect to be measured within 165–300 K. It was found that the Hall mobility was suddenly doubled at 235 K when the cubic phase was transited to the tetragonal phase (Fig. 6C). This result was well consistent with the rapid switch of TOF hole and electron mobilities during the same phase transition in $MAPbI_3$ solar cells.[28]

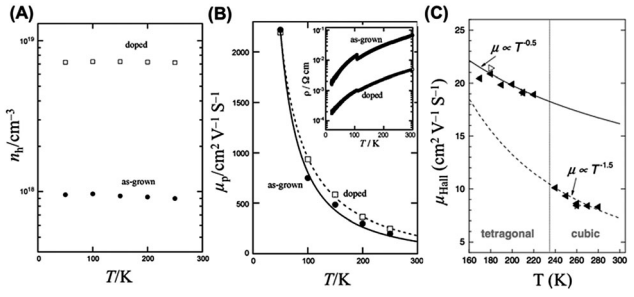

Fig. 6 Hall effect measurements of (A and B) $MASnI_3$ and (C and D) $MAPbBr_3$ single crystals. Reproduced with permission: (A and B) from ref. 34. Copyright 2013, Elsevier Inc. (C) From ref. 37. Copyright 2016, John Wiley & Sons, Inc.

The Hall effect technique is an all-round steady-state method to simultaneously acquire the bulk charge mobility, free carrier density, electrical conductivity and diffusion length of both perovskite films and single crystals. Meanwhile, the doping effect of perovskites with different chemical compositions can also be examined by this method. However, because of the equipment limitations, the Hall effect technique usually cannot measure those materials with low conductivity.

2.2.5 Space charge limited current (SCLC) technique. The SCLC technique is the most commonly used steady-state method to individually measure the hole or electron mobilities of organic semiconductors in different device architectures. This method has been used to study the charge dynamics of perovskites.

The current-density *versus* voltage (J–V) curve measured by the SCLC method is often divided into three regimes: (1) a linear ohmic regime to calculate the electrical conductivity (σ) at low bias, (2) a trap-filled regime to estimate the trap density at middle bias, and (3) a trap-free SCLC regime to determine the charge mobility at high bias. The SCLC mobility can be calculated using eqn (7):

$$J = \frac{9}{8}\mu\varepsilon_0\varepsilon_r\frac{V^2}{L^3} \quad (7)$$

where μ is the charge mobility, V is the applied voltage, ε_0 is the free space permittivity, ε_r is the dielectric constant of the perovskite, L is the separation between the electrode contacts or the thickness of the perovskite layer. In addition, the free carrier density (n) can be estimated by using the equation $n = \sigma/\mu_e$, where e is the electronic charge. Therefore, compared to the above four methods (CELIV, TOF, FET, Hall), SCLC is the simplest method because by measuring the dark J–V curves the above-mentioned basic transport parameters can be directly calculated.

The SCLC technique was mostly applied to investigate the various electronic properties of perovskite single crystals fabricated by different methods. Large SCLC hole and electron mobilities of 164 and 24.8 cm^2 V^{-1} s^{-1} were achieved in solution-grown $MAPbI_3$ single crystals, respectively.[30] The Bakr group also conducted the SCLC measurement to yield equivalently low trap densities of 5.8×10^9 and 3.3×10^{10} cm^{-3} in $MAPbBr_3$ and $MAPbI_3$ single crystals, respectively, which were grown by the anti-solvent vapor-assisted method (Fig. 7A and B).[29] The SCLC mobility of the $MAPbBr_3$ single crystals (38 cm^2 V^{-1} s^{-1}) was found an order of magnitude higher than the $MAPbI_3$ analogues (2.5 cm^2 V^{-1} s^{-1}).

The SCLC method can also be utilized to investigate the impact of phase transition on the transport properties of perovskite single crystals. For example, the Yang group unveiled the distinct transport dynamics of the black α-phase (perovskite-type) and yellow δ-phase (non-perovskite type) of $FAPbI_3$ single crystals grown by the liquid-based crystallization

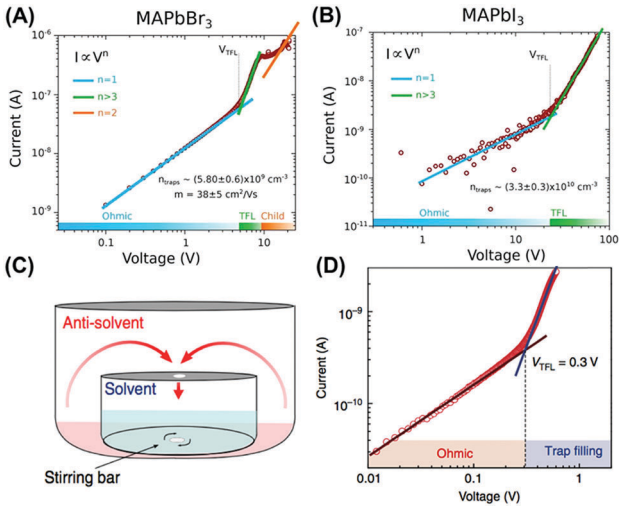

Fig. 7 SCLC measurements of (A) $MAPbBr_3$ and (B) $MAPbI_3$ single crystals grown by an anti-solvent vapor-assisted method, and (C and D) $MAPbBr_3$ planar-integrated single-crystals. Reproduced with permission: (A and B) from ref. 29. Copyright 2015, American Association for the Advancement of Science. (C and D) From ref. 39. Copyright 2015, Nature Publishing Group.

method.[38] By using SCLC measurements, a higher charge mobility (4.4 $cm^2\ V^{-1}\ s^{-1}$) and electrical conductivity ($1.1 \times 10^{-7}\ \Omega^{-1}\ cm^{-1}$) yet a lower defect concentration ($6.2 \times 10^{11}\ cm^{-3}$) and free carrier ($1.5 \times 10^{11}\ cm^{-3}$) density can be obtained in the α-phase $FAPbI_3$ single crystals than the δ-phase analogues.

However, all these above bulk perovskite single crystals are not suitable for practical device applications due to the absence of a substrate or undesirably large crystal size. In an early attempt, the Sargent and Bakr groups directly grew $MAPbBr_3$ single crystals on substrates to obtain highly crystalline films, which were termed planar-integrated single-crystal (ISC) perovskites (Fig. 7C).[39] By combination of the Hall effect and SCLC techniques, an ultrahigh charge mobility of 60 $cm^2\ V^{-1}\ s^{-1}$, a low trap density of $2 \times 10^{11}\ cm^{-3}$ and a high conductivity of $2 \times 10^{-8}\ \Omega^{-1}\ cm^{-1}$ were achieved (Fig. 7D). These results suggested that the electrical properties of ISC perovskites nearly approached those of free-standing single crystals and were much better than those of solution-processed or vapor-deposited polycrystalline films.

Therefore, SCLC is a commonly used method to determine the hole and electron mobilities of perovskites in different device architectures. Both electrical conductivity and defect densities can be simultaneously obtained by simply scanning *I–V* curves in the dark. It is worth noting that the SCLC method is only applicable to perovskites with intrinsic charge densities lower than $10^{14}\ cm^{-3}$, and therefore it is more suitable for the measurement of perovskite single crystals.

2.3 Summary

To provide an overview instruction on the selection of the technique to investigate the photo-physics in perovskite materials, we summarize the technical parameters, functionality and limitation of each above-mentioned method in Table 1. Here the time scale of the detection and the charge density needed during the measurement limit the scope of each technique for photo-physical studies. An in-depth discussion on the comparison of these techniques during the studies of photo-physics in perovskite materials will be presented in Section 4.

3. Charge carrier dynamics of perovskites

Based on these transient and steady-state measurements as discussed above, we now present an in-depth summary of the featured charge carrier dynamics of perovskites in thin films and solar cells, respectively.

3.1 Neat films

The exciton binding energy of lead halide perovskites, especially $MAPbI_3$, was found to be less than the thermal activation energy k_bT = 14–25 meV by various measurements. Consequently, the photo-generated excitons spontaneously dissociated *via* thermal activation. The kinetics of the photo-generated carrier concentration are determined by a combination of the first-order trap-state mediated charge recombination (*A*), the second-order non-geminate free carrier recombination (*B*), and the three-body Auger recombination (*C*) using eqn (8):

$$-\frac{dn}{dt} = An + Bn^2 + Cn^3, \quad (8)$$

where n is charge density and t is time. This expression can be directly verified by excitation fluency dependent TRPL studies, revealing the linear or quadratic dependence of the initial PL (denoted PL_0) intensity on the excitation density (n_0) in different excitation regimes (Fig. 8A).[10]

3.1.1 Trap mediated recombination. Under low excitation densities ($<10^{15}\ cm^{-3}$), including the conditions of working solar cells, the charge dynamics of perovskites mainly comprise both monomolecular trap-mediated and first-order geminate recombination, where the former contribution dominated owing to the long L_D of the photo-generated charges in perovskites (Fig. 8A).[11]

Therefore, the photovoltaic charge transport parameters revealed by spectroscopic studies are strongly influenced by the trap states. The dependences of trap densities on the PL lifetime have been systematically investigated (Fig. 8B–D). This includes (1) grain size (the PL lifetime of the $MAPbI_3$ polycrystalline films increased from 2 ns to 100 ns with an increment of grain sizes from <250 nm to >1 μm),[42] (2) chemical composition (the PL lifetime varied from 100 ns to 446 ns in $MAPbBr_{3-x}Cl_x$ films),[43] and (3) interfacial phenomena (the metal oxide/perovskite interfaces, for instance, would change the intrinsic PL lifetime of the neat perovskite film).[44]

3.1.2 Free carrier recombination and Auger recombination. When the excitation intensity is high ($>10^{15}\ cm^{-3}$), the second-order non-geminate recombination and the third-order Auger recombination become dominant in perovskite materials.

Table 1 Comparison of charge transport characterization techniques in perovskites

Method	Excitation pulse (s)	Probe window (s)	Charge density[o] (cm^{-3})	Output	Sample requirement and advantage	Main limitations
TA	10^{-14}–10^{-13}	10^{-13}–10^{-8} [a] 10^{-11}–10^{-4} [b]	10^{18}–10^{20}	ΔAbs,[c] τ_1[d]	No contact electrode, transparent (OD < 1)	Overlap of different spectral components
TRPL	10^{-13}–10^{-10}	10^{-12}–10^{-4}	10^{15}–10^{17}	τ_2[e]	No contact electrode, emissive sample	Only probing the emissive state
TRTS	10^{-14}–10^{-13}	10^{-12}–10^{-9}	10^{18}–10^{20}	n_h,[f] μ[g] τ_3	No contact electrode, specific substrate (*e.g.*, quartz)	Only sensitive to free charges, need theoretical model for data analysis
TRMC	10^{-13}–10^{-10}	10^{-10}–10^{-4}	10^{18}–10^{20}	n, μ, τ_3	No contact electrode, specific substrate (*e.g.*, quartz)	Only sensitive to free charges, need theoretical model for data analysis
CELIV	10^{-9}–10^{-5}	10^{-9}–10^{-6}	10^{15}–10^{17}	μ_{out}[i]	Both contact electrodes, two injection-blocking layers, applicable to working solar cells	Cannot distinguish the type of charge carrier
TOF	10^{-9}–10^{-8}	10^{-9}–10^{-6}	10^{14}–10^{15}	μ_{out}	Both contact electrodes (one must be transparent), two injection-blocking layers, measure hole and electron mobilities in the same device	Thick film (>500 nm), cannot measure in the dark
SCLC	Steady-state method		10^{10}–10^{16}	μ_{out}, σ,[j] n_{trap}[k]	Both contact electrodes, measure hole and electron mobilities in different devices	Low intrinsic charge density ($<10^{14}$ cm^{-3})
HALL				μ_{bulk},[l] n, σ, D[m]	Both contact electrodes, measure bulk charge mobility, distinguish whether n- or p-type	High electrical conductivity ($>10^{-9}$ S)
FET				μ_{in}[n]	Both contact electrodes, distinguish whether n- or p-type	High film quality to observe the obvious field effect

[a] Optical delay line. [b] Electric trigger. [c] Differential absorption. [d] Excited state lifetime. [e] Emissive state lifetime. [f] Free charge concentration. [g] Charge carrier mobility. [h] Free charge lifetime. [i] Charge mobility in the out-of-plane direction. [j] Electrical conductivity. [k] Trap density. [l] Bulk charge mobility. [m] Diffusion length. [n] Charge mobility in the in-plane direction. [o] Charge density in pump–probe measurements (TA, TRPL, TRTS, TRMC, CELIV, TOF) is calculated as the multiplication of the excitation concentration per pulse and the absorption cross section of perovskites (10^5 cm^{-1} for $MAPbI_3$), while for steady-state measurements it is defined as the charge carrier concentration during the measurement.

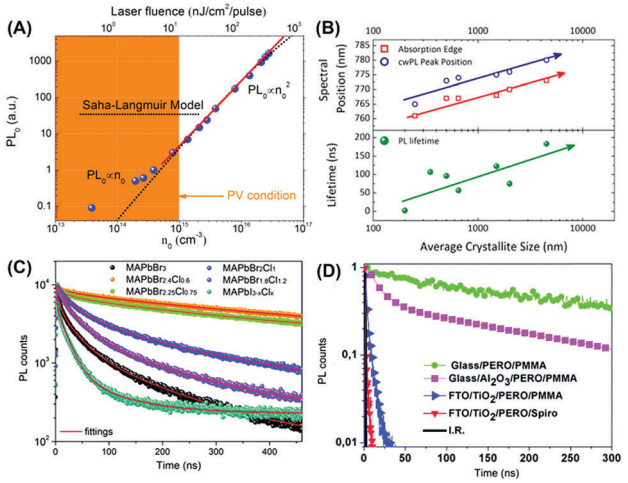

Fig. 8 (A) Dependence of PL_0 and PL kinetics on the excitation density in $MAPbBr_3$ crystals illustrating the recombination mode for the photogenerated charges. PL lifetimes for $MAPbX_3$ polycrystalline films with different (B) grain sizes, (C) halide compositions, and (D) interfacial conditions. Reproduced with permission: (B) from ref. 42. Copyright 2014, American Chemical Society. (C) From ref. 43. Copyright 2014, The Royal Society of Chemistry. (D) From ref. 44. Copyright 2014, The Royal Society of Chemistry.

The former involves the bimolecular recombination between two free charges, while the latter represents a three-body Auger process. Such higher-order charge recombination dynamics can be well observed by probing the excitation intensity dependent decay of time-resolved spectroscopy signals such as TA and TRMC.[19,21] Surprisingly, the second-order recombination rates of perovskites were found to be 2–5 orders of magnitude lower than the Langevin rate.[19,21] TRMC studies also revealed a generally low activation energy of tens of meV for the second-order recombination.[41] This was conceived as one of the photophysical origins of the low charge recombination rates in perovskite materials. Recent studies by the Savenije group suggested the direct–indirect band gap in perovskites, where the second-order recombination of mobile electrons and holes was not allowed within an indirect bandgap.[41]

3.1.3 Hot carrier dynamics. Besides the charge carrier dynamics at lower excited states near the band edge, increasing attention has been recently focused on the hot carriers in perovskites due to the slowing down of the cooling process. This may enable an efficient harvesting of hot charges to overcome the conventional thermodynamic Shockley–Queisser limit on the solar cell efficiency of ~33%.

Early studies by using TA disclosed the so-called hot-phonon bottleneck due to the substantial carrier re-absorption of optical phonons by carriers, which induces the slowing down in the cooling rate of hot charges in $MAPbI_3$ perovskites at high carrier densities.[40] Such a hot-phonon bottleneck is commonly observed in inorganic semiconductors, yet found to be much more pronounced in perovskites. This can be attributed to the decoupling between electrons and optical phonons due to the

independent motion of organic cations or internal ferroelectricity in perovskites.

Recent studies showed that even in the low carrier density regime ($<10^{17}$ cm^{-3}) far below the hot-phonon bottleneck regime, the slow hot charge cooling was still valid as evidenced by a long-lived ($\sim$100 ps) hot emission in single-crystal $MAPbBr_3$ and $FAPbBr_3$ microplates (Fig. 9A).[45] Such hot charges even transport in perovskites within a long distance ($\sim$230 nm) observed by ultrafast TA microscopy (Fig. 9B).[46] The formation of long-range polarons where photo-generated charge carriers caused by long-range lattice deformation was considered as one of the main origins. After photoexcitation, the interaction between the photogenerated charges and ionic lattices of the perovskite would induce long-range lattice deformation. Consequently, charges would be self-trapped within the lattice as polarons. The lattice deformation would screen the Coulombic interaction which is responsible for the scattering between charges and LO phonons. This would lead to a drastically reduced hot carrier cooling.

3.2 Bilayer films

Beyond neat films, perovskite materials need to be attached to charge (electron or hole) acceptors such as TiO_2, PCBM, spiro-OMeTAD and NiO to separate the photo-generated charges, which is essential for working solar cells. The charge transfer process between the perovskites and these acceptors can be visualized using different spectroscopic techniques.

Firstly, the additional depopulation pathway can be induced for excited states resulting in faster decay kinetics of the band edge bleaching PB1 in TA.[9] However, unexpected slower charge transfer times ($>$100 ps) were observed for perovskite/acceptor bilayer films using the TA technique those that of conventional photovoltaic materials (*e.g.*, organic dyes, QDs, or semiconducting polymers) where the charge injection occurred within the sub-ps timescale. Further studies showed that the TA kinetics in perovskite/acceptor systems actually represented diffusion-coupled charge transfer processes where charge diffusion in perovskite occurred before interfacial charge transfer, where the timescale ranged from 200 ps to ns. Leng *et al.* summarized the TA kinetics of perovskite/acceptor systems with various thicknesses of perovskites and extracted the electron transfer time

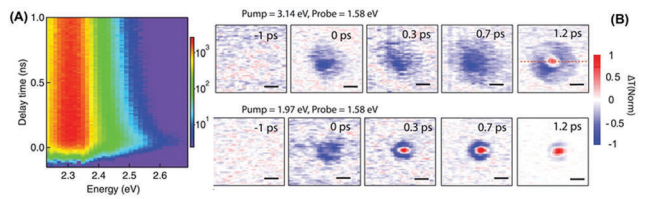

Fig. 9 (A) Hot emission observed in TRPL in single-crystal $MAPbBr_3$ microplates with a 100 ps lifetime. (B) TA microscopy images of the $MAPbI_3$ film probing the band edge carriers (excited at 1.97 eV) and hot carriers (excited at 3.14 eV). Reproduced with permission: (A) from ref. 45. Copyright 2016, American Association for the Advancement of Science. (B) from ref. 46. Copyright 2017, American Association for the Advancement of Science.

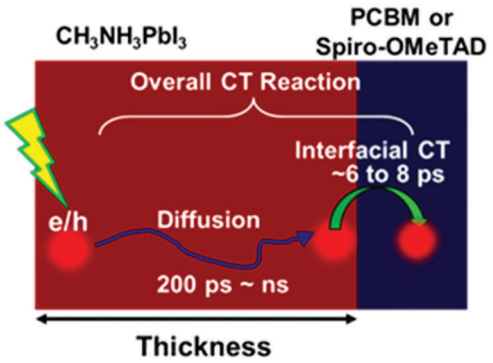

Fig. 10 Schematic illustrating charge dynamics in perovskites attached to the charge acceptor in the device configuration. Reproduced with permission from ref. 4. Copyright 2016, American Chemical Society.

to PCBM as 6 ps and the hole transfer time to spiro-OMeTAD as 8 ps (Fig. 10).[47] The long L_D prior to interfacial charge transfer can also be proven in TA in the IR range where the appearance of free charges in the acceptors can be identified as a broad IR absorption spectrum.

Secondly, distinct charge mobilities between perovskite and charge acceptors pave the way for monitoring charge transfer dynamics in perovskite/acceptor systems by TRTS. Our studies of $MAPbI_3$/mesoporous TiO_2 layers unraveled that electron injection processes were complete within 10 ps.[16] This was identified by a decrease of the initial charge mobility directly after photo-excitation in comparison to the neat perovskite in TRTS signals which featured the prompt depopulation of one species of charges either electrons or holes after charge transfer. From those studies, electron and hole mobilities can also be distinguished by considering that the TRTS mobility is a sum of both parts in the system, while the carrier mobility in the acceptors is usually orders of magnitudes lower than that in the perovskites which can be neglected in TRTS spectra. The electron mobility revealed for an $MAPbI_3$ film was comparable to or slightly higher than the hole mobility with μ_e/μ_h = 1–2, which demonstrated balanced charge transport.[16]

3.3 Working solar cells

As perovskites are organic–inorganic hybrid materials with strong light and thermal sensitivity, there remain two long-term queries about perovskite solar cells. One is why light illumination and thermally induced phase transition have a great influence on the charge transport dynamics and thus the cell performance of perovskites. The other is whether the transport properties of perovskite photovoltaics resemble those of organic or inorganic devices. In other words, it is necessary to verify whether dispersive or nondispersive charge transport, hopping or band-like conduction dominates in perovskite devices. To answer these two questions, here we not only systematically discuss the impacts of trap states and phase transition on the transport properties, but also highlight the nondispersive charge transport and band-like conduction of perovskite devices with electrodes.

3.3.1 Trap state induced light sensitivity. It is widely reported that continuous light illumination assisted in significantly

improving the PCE of PSCs. The most reliable reason is the filling of trap states under light soaking. There are various strategies to evaluate the trap states of perovskites. For example, the TOF method is a powerful transient method to make qualitative analysis about both shallow and deep trap states,[28] while the SCLC technique is a commonly used steady-state method to obtain trap densities in perovskite polycrystalline films or single crystals.[29,30] In addition, the capacitance (C)–frequency (f) technique, low-frequency noise measurements, and the spatially resolved and correlated emission/absorption method can also be applied to measure the defect densities of perovskites. Equipped with these methods, one can systematically investigate the influencing parameters of trap states in perovskites.

Although perovskites were reported to exhibit a large tolerance of trap states, we have to admit that the existence of shallow traps hinders the charge transport of PSCs. Our TOF studies of $MAPbI_3$ solar cells discovered the existence of trap-assisted recombination and direct shallow trap filling process with gradually increased hole and electron mobilities upon light soaking (Fig. 11A and B).[28] A similar conclusion was drawn by another modified CELIV measurement.[26] It was found that in both planar and mesoporous $MAPbI_3$ devices all the remaining trapped carriers disappeared after a photogeneration–extraction sequence, which suggested the absence of deep traps in perovskites.

Meanwhile, PCBM was widely reported to play an important role in passivating the interfacial trap states of perovskites. Despite that a few shallow traps were unavoidably left at the interface between $MAPbI_3$ and PCBM, the existence of PCBM intercalation often led to faster charge separation with suppressed recombination and hence higher mobility.[23] By Hall effect measurements, the PCBM layer was also found to efficiently passivate the traps of $MAPbI_3$ films, yielding a reduction of the intrinsic hole concentration and an increase of the Hall mobility of perovskites both by 3 times.[35]

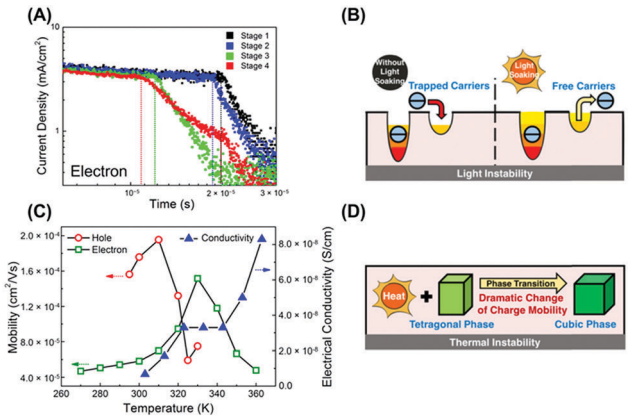

Fig. 11 Light illumination time dependent (A) TOF measurements of perovskite solar cells and (B) schematic mechanism of the trap filling process upon light soaking. Temperature dependent (C) TOF and conductivity measurements of perovskite solar cells and (D) schematic transport dynamics influenced by phase transition. Reproduced with permission: (A–D) from ref. 28. Copyright 2016, American Chemical Society.

Compared to polycrystalline films, perovskite single crystals often exhibited much lower trap densities. For instance, $MAPbX_3$ (X = Br or I) single crystals showed low conductivities around 10^8 S cm^{-1} and extremely low trap-state densities of 10^9–10^{10} cm^{-3}.[29] By contrast, the conductivity of $FAPbI_3$ single crystals was an order of magnitude higher, which was mainly attributable to the greatly increased carrier density caused by the lower bandgap of $FAPbI_3$.[38] On the other hand, owing to the self-doping effect, $MASnI_3$ exhibited metal-like high conductivity with a much higher intrinsic carrier concentration of 9×10^{17} cm^{-3} than $MAPbI_3$.[34] This indicated enormous trap states in Sn-based perovskites, which needed to be largely suppressed in order to enhance their photovoltaic performance.

More importantly, it was found that the charge transport behaviors of perovskites resembled those of inorganic semiconductors. With the aid of Hall effect measurements, carrier lifetimes and diffusion lengths were measured to be 30 ms (2.7 ms) and 23 nm (650 nm) in $MAPbI_3$ polycrystalline films and $MAPbBr_3$ single crystals, respectively, indicative of much weaker charge trapping in perovskites than most high-purity crystalline inorganic semiconductors.[36] As a result, better charge transport properties can be achieved in perovskite single crystals than polycrystalline perovskites.[29,30] Likewise, by utilizing the SCLC method, five orders of magnitude lower hole and electron trap densities were attained in MAPbI3 single crystals than in $MAPbI_3$ polycrystalline films.[30]

3.3.2 Phase transition mediated thermal sensitivity. Apart from trap states, the performance of PSCs is also greatly influenced by the operating temperature. The reason is that thermally induced phase transition can be easily triggered in perovskites and each perovskite phase possesses distinctive transport properties due to different crystalline structures.

On the one hand, a sudden change in charge mobility often occurred during the phase transition process. Our group utilized temperature dependent TOF in $MAPbI_3$/PCBM bilayer solar cells and observed rapid changes in both hole and electron mobilities when the perovskite phase change from tetragonal to cubic crystalline structures was observed (Fig. 11C and D).[28] Balanced charge transport and unchanged electrical conductivity were finally achieved during phase transition at 310–330 K, resulting in the highest PCE. A similar phenomenon was observed in the Hall measurement of $MAPbBr_3$ single crystals.[37] When the cubic phase was transited to the tetragonal phase, the Hall mobility was suddenly doubled at 235 K. It was disclosed that charge transport in the cubic phase was limited by acoustic phonon scattering rather than impurity scattering, while reduced electron–phonon scattering was achieved in the tetragonal phase owing to the suppressed rotation of the MA dipoles.

On the other hand, different perovskite phases often exhibited distinct transport properties. By SCLC measurements, it was found that higher charge mobility yet lower defect densities can be obtained in α-phase $FAPbI_3$ single crystals than Δ-phase analogues.[38] This finding explained well why only α-phase $FAPbI_3$ based solar cells afforded high PCE. By the FET method, the thermal transformation of $MAPbI_3$ microplate crystals from

n-type to ambipolar and finally to p-type semiconductor behavior was clearly observed, owing to the corresponding slight disintegration of $MAPbI_3$.[33]

3.3.3 To resemble organic or inorganic semiconductors. Although perovskites possess both organic and inorganic components, the photovoltaic behaviors such as the remarkably high charge mobility and dielectric constant render them more analogous to those of inorganic semiconductors. The strongest evidence is the observation of nondispersive charge transport in PSCs in the existence of either the PCBM layer or low temperature.

Our recent studies directly confirmed the nondispersive charge transport in $MAPbI_3$/PCBM bilayer solar cells at room temperature by observing a distinct plateau in both hole and electron TOF measurements (Fig. 11A).[28] This was distinctive from the dispersive transport among most organic solar cells, which originated often from the existence of disordered structures and deep-level traps. This result also well explained why perovskite solar cells outperformed organic counterparts, owing to the high crystallinity and large tolerance of trap states in perovskites. Similarly, by modified photo-CELIV, nondispersive electron transport was also observed in planar $MAPbI_3$ solar cells caused by the passivating function of PCBM, while dispersive electron transport was clearly observed in mesoporous perovskite devices due to the presence of traps at the TiO_2/$MAPbI_3$ interface.[27] This work further emphasized the importance of the PCBM layer in achieving a nondispersive nature in perovskite devices.

In the absence of the PCBM layer, by contrast, nondispersive charge transport can still be achieved by lowering the operating temperature. The conversion from dispersive to nondispersive charge transport at low temperature was unraveled by CELIV measurements of $MAPbI_3$/spiro-OMeTAD bilayer solar cells.[24] This behavior resulted from the suppressed trap states caused by the disordered MA dipoles at low temperature.

As organic–inorganic hybrid materials, there also remains an uncertainty about whether hopping or band-like conduction dominates in PSCs. We found that the conduction pathway was determined by not only the perovskite phases, but also the fabrication process. For instance, we unveiled that hopping and band-like conduction individually dominated in the tetragonal and cubic phases of perovskites by applying the TOF method in two-step fabricated $MAPbI_3$ solar cells (Fig. 12A).[28] By contrast, in one-step fabricated $MAPbI_3$ solar cells, the charge mobility was gradually decreased with increasing temperature by utilizing temperature-dependent CELIV, indicative of the band-like conduction in perovskites (Fig. 12B).[23] By the Hall effect measurement for $MAPbBr_3$ single crystals, a band-like transport was also verified by observing higher charge mobility at lower temperature (Fig. 12C).[37] These results indicated that the conduction type was also related to the fabrication process.

In addition, extremely low bimolecular recombination coefficients of 10^{-11}–10^{-10} cm^3 s^{-1} were found for vapor- and solution-grown $MAPbI_3$ films and $MAPbBr_3$ single crystals, which were comparable to those of the best direct-band inorganic semiconductors.[36] In addition, two orders of magnitude higher

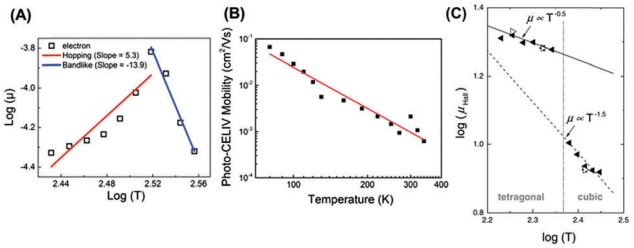

Fig. 12 Temperature dependent (A) TOF measurements of two-step fabricated $MAPbI_3$ solar cells, (B) CELIV measurements of one-step fabricated $MAPbI_3$ solar cells, and (C) Hall effect measurements of $MAPbBr_3$ single crystals. Reproduced with permission: (A) from ref. 28. Copyright 2016, American Chemical Society. (B) From ref. 23. Copyright 2015, American Chemical Society. (C) From ref. 37. Copyright 2016, John Wiley & Sons, Inc.

charge mobilities were observed in $MAPbI_3$ based FETs when the temperature was decreased below 200 K, suggesting phonon scattering-limited transport, which is similar to that of common inorganic semiconductors.[31] Therefore, all these reports verified the fact that perovskites prefer to exhibit the properties of inorganic semiconductors such as GaAs rather than the organic ones.

4. Comparison of transportation methods

Although the above-mentioned techniques are all self-consistent in elucidating the photophysics in perovskite materials individually, the comparison among those techniques exhibits a large deviation. The most critical discrepancy stems from the values of carrier mobility as measured using different transportation methods, which cover a wide range of 8 orders of magnitude as summarized in Fig. 13A (see Table S1 in the ESI†). Generally

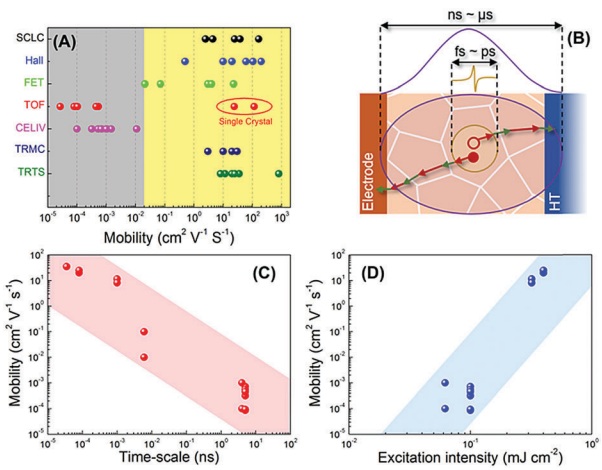

Fig. 13 (A) Charge carrier mobilities of perovskite films and single crystals measured by various techniques, (B) schematic illustrating the main detection regime of those techniques with different time windows, (C) dependence of the probing time-scale and (D) light excitation intensities on the charge mobilities obtained using different techniques for $MAPbI_xCl_{3-x}$ films.

speaking, the charge carrier mobilities in perovskites are dominated by intrinsic carrier–lattice interaction and extrinsic carrier-imperfection interaction of the materials. The former is dominated by the intrinsic electronic structures of the perovskites, while the latter reflects the charge carrier scattering by grain boundaries, dopants, lattice defects, *etc.* Putting aside the effect of sample variations including structures, morphologies, trap densities, *etc.*, which are also reported to regulate the carrier mobility by one to two orders of magnitude, we can still classify the results obtained using different techniques into two categories—mobilities extracted using the CELIV and TOF methods are usually below the level of 10^{-2} cm^2 V^{-1} s^{-1}, while the values measured using the other methods are orders of magnitude higher. Interestingly, we found that the mobilities of perovskite single crystals that were expected to be relatively defect-free, when measured in TOF, were within the same range as provided by the other methods (Fig. 13A). This indicates that the CELIV and TOF techniques are more sensitive to the long-range order of perovskites with significant contribution from the grain boundaries or interface phenomena. In contrast, other time-resolved or steady-state approaches are focused more on the local information of charge carriers.

Recent research efforts on the grain-size dependent mobilities in TRMC have already put forward similar concerns that the time scale of diffusive transport across grain boundaries in perovskites is much slower than the period of the microwave field (100 ps) which cannot be fully characterized.[48] In other words, pump–probe methods such as TRTS and TRMC tend to reflect the intrinsic capabilities of the charge transport dominated by the local acoustic photon scattering or electron–phonon scattering. In contrast, methods like CELIV and TOF with contact electrodes characterize charge carriers that undergo the entire transport period across the film structure within a much longer time scale of ns–μs (Fig. 13B). In this regard, the carrier-defect scattering, as a bottleneck for charge transport, may dominate the characteristic charge mobilities. We consider it as one of the major origins for the deviation of charge mobilities obtained from those different methods. To further support this conclusion, we summarize the dependence of charge mobilities in $MAPbI_xCl_{3-x}$ polycrystalline films on the probing time-scale (defined as the time duration of the probe pulse) measured *via* different methods in the literature (Fig. 13C). An evident decrease of mobilities accompanied by an increase of the probing time-scale can be observed, which is consistent with our assumption. It should also be noted that in steady-state measurements (SCLC and Hall effect), the inter-grain and cross-grain transportation of charge carriers can be well distinguished by modulating the applied voltage or magnetic field. Therefore, the charge mobilities extracted using those methods can still be close to those obtained using the TRTS and TRMC methods.

Another crucial factor to be accounted for is the photo-excitation intensities, which also determine the carrier concentration in perovskites. According to classic semiconductor physics, the carrier mobility is reverse to the charge scattering rates (γ). In principle, γ would increase as a function of the carrier concentration in a semiconductor due to the increased carrier–carrier scattering, which leads to a reduction of charge mobility.[49] However, the summarized dependences between excitation intensities and mobilities measured *via* various techniques for perovskite materials exhibit the opposite trend (Fig. 13D). One plausible explanation is the dynamic trap filling process at high carrier densities, which diminishes the carrier–defect scattering of residual free carriers. Such trap filling has been widely observed in perovskite materials, indicating that the carrier concentration not only mediates the recombination mode of the photo-generated charges (*i.e.*, first-order or higher-order charge recombination) but also determines the effective defect densities at excited states.[50]

Besides that, the analysis methodologies of each technique would also result in a deviation of the output. As mentioned above, for instance, the analysis of AC conductivity in TRTS and TRMC required comprehensive physical models which may vary by the geometries of the samples and the experimental configurations. In addition, the possible lattice deformation at excited states by polaron formation or photo-induced ferroelectricity could also lead to different charge carrier dynamics measured between the dark state methods (*e.g.*, FET, Hall effect) and the methods with light excitation.

There remains a long-standing debate concerning which method is more appropriate to rationalize the photo-physical origins of the superior photovoltaic performance of perovskite materials. The above comparisons suggest that various steady-state, transient and ultrafast techniques are indeed complementary to each other, at least in determining carrier mobilities. In brief, the capability of transporting photo-generated charge carriers is dominated by several scattering processes including (1) carrier–phonon, (2) carrier–carrier, (3) carrier–plasmon, and (4) carrier–impurity scattering. Different techniques presented in this review only characterize some of those processes depending on the above-mentioned transport parameters. Therefore, it is a risk to interpret the charge dynamics of perovskites by using one single technique without specifying the detection regime. In order to characterize the entire charge transport process within perovskites from charge photo-generation, separation to collection, a combination of multiple approaches is highly needed.

5. Conclusions

This review systematically introduced the charge transport dynamics of perovskites, which were investigated using various techniques including ultrafast spectroscopies (TA, TRPL, TRTS, TRMC), transient electrical measurements (CELIV, TOF), and steady-state methods (FET, Hall effect, SCLC). Followed by a brief introduction of each technique, we summarized representative results of perovskites in the literature obtained from those transportation methods in terms of carrier mobilities, lifetimes, diffusion lengths, *etc.* From these results, most of the critical charge carrier dynamics are gained in neat films, bilayer

films and operating solar cells based on perovskites. In neat films, photo-generated species are predominantly contributed by free carriers which mainly undergo trap-assisted first-order recombination. In conjunction with the charge acceptor to form the bilayer films, the interfacial charge transfer is generally efficient within the picosecond time-scale. In real device configurations, the charge transport is non-dispersive and dominated by the band-like conduction which also exhibits large trap tolerance.

More importantly, we manifested the difference and limitation of each technique in the photo-physical studies of perovskite materials. We showed that due to various time windows and excitation levels, these techniques are sensitive to specific processes during charge transport. Ultrafast spectroscopies with high excitation concentrations and relatively short time-windows tend to probe the local charge carrier dynamics that are determined by the intrinsic structures of the perovskites, while transient electrical measurements with long time-windows and low excitation intensities detect the collective charge transport behaviors with large contribution from the grain boundaries and interface phenomena within the perovskites. We also emphasize the complementary points of view that integrate the different techniques to rationalize the solar cell performance using photo-physical studies.

Acknowledgements

Z. L. thanks the support from the National Natural Science Foundation of China (NSFC) under grant no. 51473036. K. Z. and T. P. acknowledges the support from the Swedish Research Council, the KAW Foundation, the NPRP grant #NPRP7-227-1-034 obtained from the Qatar National Research Fund (a member of the Qatar Foundation), and the STINT grant #CH2015-6232 from the Swedish Foundation for International Cooperation in Research and Higher Education.

Notes and references

1 Best Research Cell Efficiencies: http://www.nrel.gov/ncpv/images/efficiency_chart.jpg, accessed in March 2017.
2 T. C. Sum, N. Mathews, G. Xing, S. S. Lim, W. K. Chong, D. Giovanni and H. A. Dewi, *Acc. Chem. Res.*, 2016, **49**, 294–302.
3 X. Wu, M. T. Trinh, D. Niesner, H. Zhu, Z. Norman, J. S. Owen, O. Yaffe, B. J. Kudisch and X.-Y. Zhu, *J. Am. Chem. Soc.*, 2015, **137**, 2089–2096.
4 S. Narra, C.-C. Chung, E. W.-G. Diau and S. Shigeto, *J. Phys. Chem. Lett.*, 2016, **7**, 2450–2455.
5 K. G. Stamplecoskie, J. S. Manser and P. V. Kamat, *Energy Environ. Sci.*, 2015, **8**, 208–215.
6 S. D. Stranks, G. E. Eperon, G. Grancini, C. Menelaou, M. J. P. Alcocer, T. Leijtens, L. M. Herz, A. Petrozza and H. J. Snaith, *Science*, 2013, **342**, 341–344.
7 Y. Yang, Y. Yan, M. Yang, S. Choi, K. Zhu, J. M. Luther and M. C. Beard, *Nat. Commun.*, 2015, **6**, 7961.
8 Z. Guo, J. S. Manser, Y. Wan, P. V. Kamat and L. Huang, *Nat. Commun.*, 2015, **6**, 7471.
9 G. Xing, N. Mathews, S. Sun, S. S. Lim, Y. M. Lam, M. Grätzel, S. Mhaisalkar and T. C. Sum, *Science*, 2013, **342**, 344–347.
10 M. Saba, M. Cadelano, D. Marongiu, F. Chen, V. Sarritzu, N. Sestu, C. Figus, M. Aresti, R. Piras, A. G. Lehmann, C. Cannas, A. Musinu, F. Quochi, A. Mura and G. Bongiovanni, *Nat. Commun.*, 2014, **5**, 5049.
11 J.-C. Blancon, W. Nie, A. J. Neukirch, G. Gupta, S. Tretiak, L. Cognet, A. D. Mohite and J. J. Crochet, *Adv. Funct. Mater.*, 2016, **26**, 4283–4292.
12 L. M. Pazos-Outón, M. Szumilo, R. Lamboll, J. M. Richter, M. Crespo-Quesada, M. Abdi-Jalebi, H. J. Beeson, M. Vrućinić, M. Alsari, H. J. Snaith, B. Ehrler, R. H. Friend and F. Deschler, *Science*, 2016, **351**, 1430–1433.
13 D. A. Valverde-Chávez, C. S. Ponseca, C. C. Stoumpos, A. Yartsev, M. G. Kanatzidis, V. Sundström and D. G. Cooke, *Energy Environ. Sci.*, 2015, **8**, 3700–3707.
14 C. La-o-vorakiat, T. Salim, J. Kadro, M.-T. Khuc, R. Haselsberger, L. Cheng, H. Xia, G. G. Gurzadyan, H. Su, Y. M. Lam, R. A. Marcus, M.-E. Michel-Beyerle and E. E. M. Chia, *Nat. Commun.*, 2015, **6**, 7903.
15 R. L. Milot, G. E. Eperon, H. J. Snaith, M. B. Johnston and L. M. Herz, *Adv. Funct. Mater.*, 2015, **25**, 6218–6227.
16 C. S. Ponseca, T. J. Savenije, M. Abdellah, K. Zheng, A. Yartsev, T. R. Pascher, T. Harlang, P. Chabera, T. Pullerits, A. Stepanov, J.-P. Wolf and V. Sundström, *J. Am. Chem. Soc.*, 2014, **136**, 5189–5192.
17 C. Wehrenfennig, G. E. Eperon, M. B. Johnston, H. J. Snaith and L. M. Herz, *Adv. Mater.*, 2014, **26**, 1584–1589.
18 Y. Chen, Y. Sun, J. Peng, W. Zhang, X. Su, K. Zheng, T. Pullerits and Z. Liang, *Adv. Energy Mater.*, 2017, 1700162.
19 C. Colbeau-Justin and M. A. Valenzuela, *Rev. Mex. Fis.*, 2013, **59**, 191–200.
20 H. Oga, A. Saeki, Y. Ogomi, S. Hayase and S. Seki, *J. Am. Chem. Soc.*, 2014, **136**, 13818–13825.
21 E. M. Hutter, G. E. Eperon, S. D. Stranks and T. J. Savenije, *J. Phys. Chem. Lett.*, 2015, **6**, 3082–3090.
22 Y. Bi, E. M. Hutter, Y. Fang, Q. Dong, J. Huang and T. J. Savenije, *J. Phys. Chem. Lett.*, 2016, **7**, 923–929.
23 Y. Chen, J. Peng, D. Su, X. Chen and Z. Liang, *ACS Appl. Mater. Interfaces*, 2015, **7**, 4471–4475.
24 R. T. Ginting, E.-S. Jung, M.-K. Jeon, W.-Y. Jin, M. Song and J.-W. Kang, *Nano Energy*, 2016, **27**, 569–576.
25 H. Tsai, W. Nie, J.-C. Blancon, C. C. Stoumpos, R. Asadpour, B. Harutyunyan, A. J. Neukirch, R. Verduzco, J. J. Crochet, S. Tretiak, L. Pedesseau, J. Even, M. A. Alam, G. Gupta, J. Lou, P. M. Ajayan, M. J. Bedzyk, M. G. Kanatzidis and A. D. Mohite, *Nature*, 2016, **536**, 312–316.
26 Q. Lin, A. Armin, R. C. R. Nagiri, P. L. Burn and P. Meredith, *Nat. Photonics*, 2015, **9**, 106–112.
27 M. Petrović, T. Ye, C. Vijila and S. Ramakrishna, *Adv. Energy Mater.*, 2017, 1602610.
28 J. Peng, Y. Sun, Y. Chen, Y. Yao and Z. Liang, *ACS Energy Lett.*, 2016, **1**, 1000–1006.

29 D. Shi, V. Adinolfi, R. Comin, M. Yuan, E. Alarousu, A. Buin, Y. Chen, S. Hoogland, A. Rothenberger, K. Katsiev, Y. Losovyj, X. Zhang, P. A. Dowben, O. F. Mohammed, E. H. Sargent and O. M. Bakr, *Science*, 2015, **347**, 519–522.
30 Q. Dong, Y. Fang, Y. Shao, P. Mulligan, J. Qiu, L. Cao and J. Huang, *Science*, 2015, **347**, 967–970.
31 X. Y. Chin, D. Cortecchia, J. Yin, A. Bruno and C. Soci, *Nat. Commun.*, 2015, **6**, 7383.
32 M.-J. Zhang, N. Wang, S.-P. Pang, Q. Lv, C.-S. Huang, Z.-M. Zhou and F.-X. Ji, *ACS Appl. Mater. Interfaces*, 2016, **8**, 31413–31418.
33 D. Li, H.-C. Cheng, Y. Wang, Z. Zhao, G. Wang, H. Wu, Q. He, Y. Huang and X. Duan, *Adv. Mater.*, 2016, **29**, 1601959.
34 Y. Takahashi, H. Hasegawa, Y. Takahashi and T. Inabe, *J. Solid State Chem.*, 2013, **205**, 39–43.
35 Z. Xiao, C. Bi, Y. Shao, Q. Dong, Q. Wang, Y. Yuan, C. Wang, Y. Gao and J. Huang, *Energy Environ. Sci.*, 2014, **7**, 2619–2623.
36 Y. Chen, H. T. Yi, X. Wu, R. Haroldson, Y. N. Gartstein, Y. I. Rodionov, K. S. Tikhonov, A. Zakhidov, X.-Y. Zhu and V. Podzorov, *Nat. Commun.*, 2016, **7**, 12253.
37 H. T. Yi, X. Wu, X. Zhu and V. Podzorov, *Adv. Mater.*, 2016, **28**, 6509–6514.
38 Q. Han, S.-H. Bae, P. Sun, Y.-T. Hsieh, Y. M. Yang, Y. S. Rim, H. Zhao, Q. Chen, W. Shi, G. Li and Y. Yang, *Adv. Mater.*, 2016, **28**, 2253–2258.
39 M. I. Saidaminov, V. Adinolfi, R. Comin, A. L. Abdelhady, W. Peng, I. Dursun, M. Yuan, S. Hoogland, E. H. Sargent and O. M. Bakr, *Nat. Commun.*, 2015, **6**, 8724.
40 M. B. Price, J. Butkus, T. C. Jellicoe, A. Sadhanala, A. Briane, J. E. Halpert, K. Broch, J. M. Hodgkiss, R. H. Friend and F. Deschler, *Nat. Commun.*, 2015, **6**, 8420.
41 E. M. Hutter, M. C. Gélvez-Rueda, A. Osherov, V. Bulovic, F. C. Grozema, S. D. Stranks and T. J. Savenije, *Nat. Mater.*, 2017, **16**, 115–120.
42 V. D'Innocenzo, A. R. Srimath Kandada, M. De Bastiani, M. Gandini and A. Petrozza, *J. Am. Chem. Soc.*, 2014, **136**, 17730–17733.
43 M. Zhang, H. Yu, M. Lyu, Q. Wang, J.-H. Yun and L. Wang, *Chem. Commun.*, 2014, **50**, 11727–11730.
44 V. Roiati, S. Colella, G. Lerario, L. D. Marco, A. Rizzo, A. Listorti and G. Gigliade, *Energy Environ. Sci.*, 2014, **7**, 1889–1894.
45 H. Zhu, K. Miyata, Y. Fu, J. Wang, P. P. Joshi, D. Niesner, K. W. Williams, S. Jin and X.-Y. Zhu, *Science*, 2016, **353**, 1409–1413.
46 Z. Guo, Y. Wan, M. Yang, J. Snaider, K. Zhu and L. Huang, *Science*, 2017, **356**, 59–62.
47 J. Leng, J. Liu, J. Zhang and S. Jin, *J. Phys. Chem. Lett.*, 2016, **7**, 5056–5061.
48 O. G. Reid, M. Yang, N. Kopidakis, K. Zhu and G. Rumbles, *ACS Energy Lett.*, 2016, **1**, 561–565.
49 H. J. Joyce, J. Wong-Leung, C.-K. Yong, C. J. Docherty, S. Paiman, Q. Gao, H. H. Tan, C. Jagadish, J. Lloyd-Hughes, L. M. Herz and M. B. Johnston, *Nano Lett.*, 2012, **12**, 5325–5330.
50 S. D. Stranks, V. M. Burlakov, T. Leijtens, J. M. Ball, A. Goriely and H. J. Snaith, *Phys. Rev. Appl.*, 2014, **2**, 034007.